

Convective Forcing in the Intertropical Convergence Zone of the Eastern Pacific

DAVID J. RAYMOND AND G. B. RAGA

Universidad Nacional Autónoma de México, Mexico City, Mexico

CHRISTOPHER S. BRETHERTON

University of Washington, Seattle, Washington

JOHN MOLINARI

University at Albany, State University of New York, Albany, New York

CARLOS LÓPEZ-CARRILLO AND ŽELJKA FUCHS

New Mexico Institute of Mining and Technology, Socorro, New Mexico

(Manuscript received 9 July 2002, in final form 14 April 2003)

ABSTRACT

One of the goals of the East Pacific Investigation of Climate, year 2001 process study (EPIC2001), was to understand the mechanisms controlling the forcing of deep atmospheric convection over the tropical eastern Pacific. An intensive study was made of convection in a $4^\circ \times 4^\circ$ square centered on 10°N , 95°W in September and October of 2001. This is called the intertropical convergence zone (ITCZ) study region because it encompasses the eastern Pacific intertropical convergence zone. Starting from an analysis of the theoretical possibilities and a plethora of dropsonde, in situ, radar, and satellite data, it is found that newly developing convection occurs where a deep layer of air (of order 1 km deep or deeper) is conditionally unstable with only weak convective inhibition. Shallower conditionally unstable layers are associated with numerous small clouds, but do not seem to produce deep convection.

The occurrence of deep convection over the ITCZ study region is presumably related to the propensity of the environment to produce areas of weak convective inhibition over such a deep layer. Three theoretically possible factors control the formation of such convectively unstable areas: 1) the strength of the total surface heat (or moist entropy) fluxes; 2) the advection of moisture into the region; and 3) temperature anomalies caused by dry adiabatic ascent of the inhibition layer, which lies typically between 700 and 850 mb. The areal fraction covered by such instability is small even on highly convective days.

In the tropical eastern Pacific, it is found that the total surface entropy flux is the most significant of these factors, with a warm layer in the 700–850-mb range, resulting presumably from subsidence, playing an important suppressive role in certain cases. These two factors account for approximately two-thirds of the variance in satellite infrared brightness temperature averaged over the study region. Moisture (or moist entropy) advection appears to be of less importance. Tropical disturbances such as easterly waves, Kelvin waves, and the Madden–Julian oscillation presumably control convection primarily via these two mechanisms during their passage through this region.

1. Introduction

After many years of study, we know surprisingly little about the mechanisms responsible for the control by the large scale of deep convection over warm tropical oceans. This deficiency compromises our ability to make weather and climate predictions in these regions.

Few systematic measurements have been made in the

eastern tropical Pacific. Dropsondes were deployed in the region during the First Global Atmospheric Research Program (GARP) Global Experiment (FGGE; Firestone and Albrecht 1986; Kloesel and Albrecht 1989; Yin and Albrecht 2000). The tropical atmosphere–ocean (TAO) moorings along 95°W were installed during the period 1992 to 1994. These, of course, only produce surface atmospheric measurements. An intensive aircraft study of developing tropical cyclones in the eastern Pacific was made during the Tropical Experiment in Mexico (TEXMEX) in the summer of 1991 (Bister and Emanuel 1997; Raymond et al. 1998). In September 1996 an aircraft study of conditions over the cold water regions

Corresponding author address: Dr. David J. Raymond, Physics Department, New Mexico Institute of Mining and Technology, 801 Leroy Place, Socorro, NM 87801-4796.
E-mail: raymond@kestrel.nmt.edu

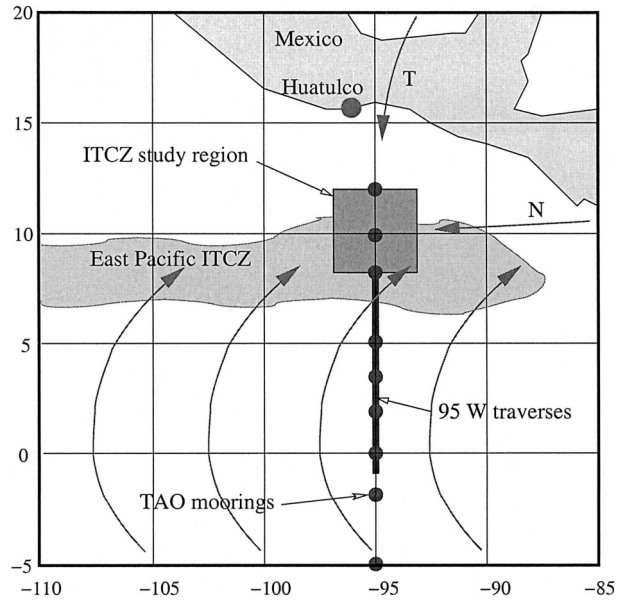


FIG. 1. Map of the eastern tropical Pacific showing the ITCZ, general surface flows, locations of TAO moorings and the ITCZ study region, and the aircraft base in Huatulco, Mexico. The arrows labeled T and N represent sporadic gap flows through the Isthmus of Tehuantepec and the lowlands of Nicaragua.

of the eastern Pacific near and south of the equator was made (Paluch et al. 1999). Oceanographic and atmospheric measurements were made south of Acapulco in three 10-day cruises of the Mexican oceanographic vessel *Puma* during the summer of 2001 (V. Magaña 2001, personal communication).

Unfortunately, none of the above programs (with the possible exception of the *Puma* cruises, the results of which were not available at the time of writing) provided the type of systematic data needed to assess the conditions under which deep convection occurs in the eastern Pacific intertropical convergence zone (ITCZ) region.

The East Pacific Investigation of Climate, year 2001 process study (EPIC2001) was designed to learn more about processes in the eastern Pacific that are handled poorly by climate models. Among these are deep atmospheric convection in the ITCZ over the Mexican warm pool, a region of warm surface waters extending south from the Mexican and Central American Pacific coast to within a few degrees of the equator. Intensive observations made during this project have the potential to reveal how deep convection is driven, at least in this region of the world.

The field phase of EPIC2001 was carried out in September and October of 2001 (Raymond et al. 2003, manuscript submitted to *Bull. Amer. Meteor. Soc.*). Two research aircraft, the C-130 of the National Center for Atmospheric Research (NCAR) and a P-3 belonging to the National Oceanic and Atmospheric Administration (NOAA) were based in Huatulco, Mexico, in support of EPIC2001. This location allowed the aircraft to ex-

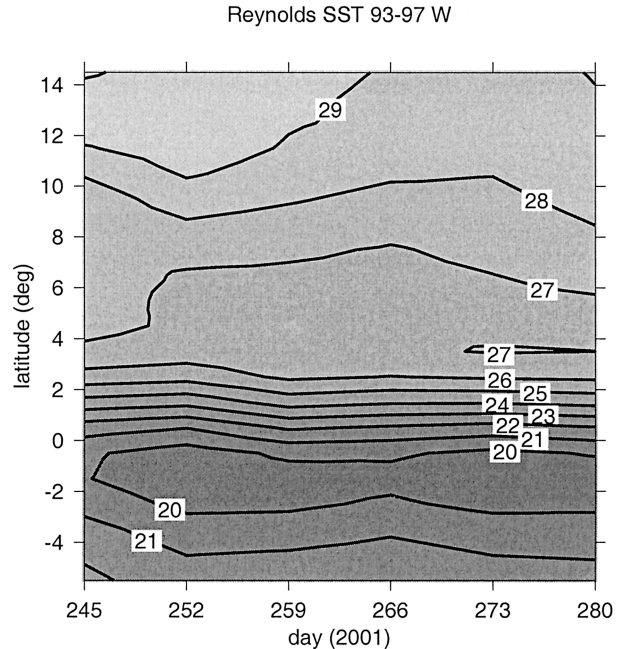


FIG. 2. Reynolds SST ($^{\circ}\text{C}$) as a function of latitude and time during the EPIC2001 project, averaged from 93° to 97°W .

plore conditions along and near the 95°W TAO mooring line (McPhaden 1995; see Fig. 1). Collocation of EPIC2001 observations with observations from these moorings was made to help in the interpretation of the long-term but less comprehensive mooring measurements. Moorings were added especially for EPIC2001 at 3.5°N , 10°N , and 12°N . All moorings along 95°W were enhanced with pressure sensors and a variety of other instrumentation.

In addition to the aircraft and enhanced TAO moorings, two ships, NOAA's R/V *Ron Brown* and the ship R/V *New Horizon* belonging to the National Science Foundation (NSF), made atmospheric and oceanic measurements near 10°N , 95°W during part of the observational period and later traversed the 95°W line.

Aircraft observations were made along the 95°W line from 12°N to 1°S by the C-130 in order to monitor the cross-equatorial inflow into the ITCZ. In addition, intensive aircraft measurements were made by the C-130 and the P-3 in an ITCZ study region bounded by 8° – 12°N and 93° – 97°W .

Figure 2 shows the SST in the eastern Pacific during the field phase of EPIC2001 as a function of latitude and time. The SST is that produced by Reynolds (1988) and Reynolds and Marsico (1993) and is averaged in longitude from 93°W to 97°W . A significant north–south SST gradient exists even well north of the SST front, which was near the equator during the EPIC2001 field program. Simple hydrostatic arguments (e.g., Riehl et al. 1951; Lindzen and Nigam 1987; etc.) suggest that an atmospheric pressure gradient should exist at low levels over an SST gradient in the sense that drives low-

level air toward warmer SSTs. The eastern Pacific SST gradient does indeed drive a low-level southerly flow, which carries air across the equator and into the eastern Pacific ITCZ (see, e.g., Yin and Albrecht 2000).

EPIC2001 observations provide a plethora of data pertinent to the issue of convective forcing over tropical oceans. The purpose of this paper is to use EPIC2001 data to uncover the factors controlling the existence and variability of deep convection in the eastern Pacific ITCZ. Section 2 discusses possible convective forcing mechanisms over tropical oceans which may be applicable to the eastern Pacific. Section 3 describes the data sources used in this analysis. In section 4 we examine the immediate factors responsible for the development of new convection in the EPIC2001 region, while in section 5 we evaluate alternative theories of higher-order convective forcing mechanisms that act indirectly via the above direct mechanisms. Conclusions are presented in section 6.

2. Convective forcing mechanisms

One of the most difficult aspects of the study of convection over tropical oceans is tracing the thread of causality. Whereas many factors such as low-level convergence, strong surface fluxes, column-integrated moisture, etc., are often correlated with deep convection, it is difficult to determine whether these factors cause the convection, are consequences of it, or are simply incidental. Theoretical reasoning supported by careful observation and modeling seems to be the only path out of this dilemma.

We know some things with great certainty. In particular, we probably all agree that convection is ultimately forced by those factors controlling the release of conditional instability. Thus, convection occurs when CIN is small enough for triggering in the form of small-scale lifting mechanisms universally present in the environment to carry parcels upward to the level of free convection. In an instantaneous sense, the amount of convection is determined by the vigor and amount of small-scale lifting. The character of the resulting convection is then determined by the size of the lifted parcel (and the resulting entrainment rate), the shear, temperature, and humidity profiles of the local environment, as well as the aerosol content of the atmosphere, with the latter affecting the nature of precipitation produced by the convection.

Beyond these points our knowledge becomes less firm. Over the open ocean, mechanisms causing the initial small-scale lifting of parcels are generally limited to boundary layer turbulence, mesoscale rolls and cells, and disturbances such as gust fronts associated with preexisting convection. The orographic effects and differential heating that are so effective at driving convection over land are absent. Thus, with no preexisting convection, lifting of near-surface parcels is weak,

which means that such parcels reach the level of free convection (LFC) only if CIN is small.

It is awkward if not impossible to incorporate direct convective triggering into large-scale models of the atmosphere, so intermediate mechanisms are generally sought that are thought to mediate the release of conditional instability and that can be related to large-scale variables.

Three types of intermediate mechanisms can change low-level environmental profiles, and hence the CIN: 1) large-scale dry adiabatic lifting or subsidence near cloud base, 2) differential advection of moisture or temperature, and 3) diabatic or turbulent processes that alter the vertical distribution of temperature and humidity.

In the first category, one can imagine lifting by slow manifold processes such as quasigeostrophic dynamics, inertia-gravity or Kelvin waves, and Ekman pumping.

The second category is sometimes manifested as convective suppression by the import of dry air from distant regions such as the subtropics (Parsons et al. 2000). However, the reverse process could also occur, in which convection is enhanced by the advective import of very moist air. Little temperature advection should occur in the Tropics due to the typically weak horizontal temperature gradients there.

In the third category are direct radiative effects and the vertical redistribution of surface moist entropy fluxes.

Frequent use of the specific moist entropy and the saturated specific moist entropy are made in this paper because entropy has better conservation characteristics in moist processes than any of the usual definitions of equivalent potential temperature, or of moist static energy.¹ However, plots of entropy and saturated entropy can be interpreted qualitatively as one would interpret plots of equivalent potential temperature and saturated equivalent potential temperature.

Large-scale lifting acts to force convection in the following manner. Dry adiabatic ascent near cloud base cools the air there relative to the surface, which has the effect of reducing the CIN. More convection then presumably occurs, with compensating subsidence developing in the region immediately surrounding the convection. This subsidence warms the air, increasing CIN. In equilibrium these two factors balance. If there are no precipitation-generated downdrafts, the large-scale upward mass flux at cloud base is realized almost entirely as convective updraft mass flux at this level, and there is, on the average, no vertical motion outside moist up-

¹ The moist entropy is approximately conserved even when warm rain removes water substance, since the specific entropy of liquid water at 0°C is zero with the usual choice of constants (see Raymond and Blyth 1992). Unfortunately, the reversible equivalent potential temperature of Emanuel (1994) is a function of both the entropy and the total water mixing ratio, so it does not share the conservative properties of the entropy in the presence of liquid precipitation. Moist static energy is only conserved when hydrostatic balance holds precisely in updrafts and downdrafts.

drafts aside from that produced by radiatively induced subsidence.

When the proviso of no moist downdrafts is relaxed, the picture changes dramatically. Zipser (1969, 1977) found that deep convection over tropical oceans generated downdrafts of rain-cooled air, which brought large quantities of low entropy air to the surface. This air is highly stable in the sense that no reasonable lifting will result in the release of conditional instability. Thus, once all boundary layer air is displaced by downdraft air in some region, no further deep convection is possible until surface latent and sensible heat fluxes reenergize this air, a process which takes typically 12–24 h.

Since surface fluxes are roughly proportional to the surface wind speed, flux-based boundary layer regeneration is more a function of the distance traveled across the surface by boundary layer parcels rather than of elapsed time. Raymond (1995) estimated that a fully exhausted subcloud layer typically needs to travel about 250 km in contact with a warm ocean to regenerate via surface fluxes, which takes about 14 h at 5 m s⁻¹. If a deeper layer needs to be restored, a proportionately longer trajectory is required.

Convection itself may increase surface moist entropy fluxes by virtue of the gusty winds and the low entropy of downdraft air generally found in convection's vicinity (Saxen and Rutledge 1998). This may have an amplifying effect on convection produced by a preexisting surface flux anomaly. In the extreme case one could imagine a self-exciting convective disturbance that supports itself by self-generated fluxes. Hurricanes work this way (Malkus and Riehl 1960; Emanuel 1986; Rotunno and Emanuel 1987). However, short of this possibility, the arrow of causality still points from the preexisting anomaly to the convection, as the convective enhancement of the fluxes would not exist without the initial forcing of convection.

Once a parcel reaches the LFC, free tropospheric environmental effects become important. The existence of large convective available potential energy (CAPE) and high relative humidity are generally thought to result in stronger and deeper convection, while wind shear may either help or hurt, depending on the circumstances (LeMone et al. 1998; Lucas and Zipser 2000; Lucas et al. 2000).

In the context of forcing of convection by surface entropy fluxes, a key parameter is the amount of low entropy downdraft air injected into the boundary layer per unit of updraft mass flux (Raymond 1995; Emanuel 1995). For equilibrium between surface fluxes and convection, the negative entropy tendency in the boundary layer due to downdrafts must balance the positive entropy tendency due to surface fluxes:

$$m_d(s_b - s_d) = \rho_b U_b C_D (s_{ss} - s_b), \quad (1)$$

where m_d is the mass per unit area per unit time of downdraft air entering the boundary layer from above, s_d is the specific entropy of the downdraft air, s_b is the

specific entropy of the boundary layer, s_{ss} is the saturated specific entropy at the temperature and pressure of the sea surface, ρ_b is the air density in the boundary layer, U_b is the wind speed there, and $C_D \approx 10^{-3}$ is the exchange coefficient.

Defining the ratio of downdraft to updraft mass flux at the top of the boundary layer as $\alpha = m_d/m_u$, we find that the equilibrium updraft mass flux at the top of the boundary layer is

$$m_u = \frac{\rho_b U_b C_D (s_{ss} - s_b)}{\alpha (s_b - s_d)}. \quad (2)$$

Thus, for a given surface entropy flux, the updraft mass flux is greater if the ratio of downdraft to updraft mass flux α is smaller.

The quantity α is not a constant of nature, but is presumably a function of the environment in which convection occurs. One might imagine that a moister environment with lower shear would result in lower values of α , but the natural variability of this parameter has yet to be studied.

Raymond (1995) denoted the theory arising from the assumed balance between convective downdrafts and surface fluxes *boundary layer quasi-equilibrium* (BLQ), with “boundary layer” indicating the subcloud layer. In the presence of typical oceanic small clouds with 1–2-km tops, it may make more sense to consider the boundary layer to include both the subcloud layer and the shallow cloud layer, as considerable mixing can occur through this deeper region.

Note that for simplicity we have ignored the direct radiative effect on the boundary layer entropy, the clear air entrainment of free tropospheric air into the boundary layer, and the lateral detrainment of entropy. A full analysis of the entropy budget of a layer is now given, which takes these terms into account.

Consider a box of horizontal area A and periphery P bounded below by the ocean surface and above by a horizontal surface. The pressure thickness of this box is assumed to be Δp . Ignoring the irreversible generation of entropy, the tendency of the mean entropy in the box is given by

$$\frac{ds'}{dt} = \frac{g\overline{F}_{ss}}{\Delta p} + \underline{R}_s - \frac{P\langle s'u_n \rangle}{A} - \frac{g\rho\overline{s'w}}{\Delta p}, \quad (3)$$

where g is the acceleration of gravity, $s' = s - s_R$ is the perturbation of the entropy from a constant reference value s_R , F_{ss} is the flux of entropy from the sea into the air, R_s is the radiative source of entropy, u_n is the outward normal component of the air velocity on the lateral surface of the box, w is the vertical air velocity on the box top, and ρ is the mean density there. An underline indicates an average over the box volume, an overline an average over the horizontal area of the box, and angle brackets an average of the box's lateral faces. Mass continuity is given by

TABLE 1. Information about EPIC2001 research flights. The day is computed so that 0000 UTC on 1 Jan 2001 has a value of 1.0. In the mission column, “ITCZ” indicates a study in the ITCZ study region using either the P-3 or the C-130 or both, “95°W” indicates a C-130 traverse of 95°W, and “SST” indicates a C-130 study of the SST front near the equator. The names in capital letters under comments indicate tropical storm passages. IRIS was an Atlantic tropical storm, the remnants of which passed overhead. P-3 flight 010928I was aborted due to engine failure. Flight 010921I was an operational flight into Tropical Storm Juliette.

Day	Date	Mission	P-3	C-130	Comment
246	3 Sep	1 - ITCZ	010903I	RF01	
248	5	2 - ITCZ	010905I	RF02	
250	7	3 - 95W	010907I	RF03	
252	9	4 - ITCZ	010909I	RF04	IVO
256	13	5 - ITCZ	010913I	RF05	
257	14	6 - 95°W		RF06	
259	16	7 - ITCZ	010916I	RF07	KIKO south
262	19	8 - 95°W		RF08	
263	20	9 - ITCZ	010920I	RF09	JULIETTE east
264	21	Operational	010921I		JULIETTE
266	23	10 - 95°W		RF10	JULIETTE west
268	25	11 - 95°W		RF11	
271	28	12 - ITCZ	(010928I)	RF12	LORENA west
272	29	13 - ITCZ		RF13	LORENA west
275	2 Oct	14 - 95°W		RF14	
276	3	15 - ITCZ/SST	011003I	RF15	
278	5	16 - ITCZ/SST	011005I	RF16	
279	6	17 - ITCZ	011006I	RF17	
280	7	18 - ITCZ	011007I		
282	9	19 - 95°W		RF18	IRIS over Huatulco
283	10	20 - 95°W		RF19	

$$\frac{P\langle u_n \rangle}{A} + \frac{g\rho\bar{w}}{\Delta p} = 0. \quad (4)$$

Equation (3) adds the effects of horizontal advection and radiation to the simplified entropy balance presented in (1).

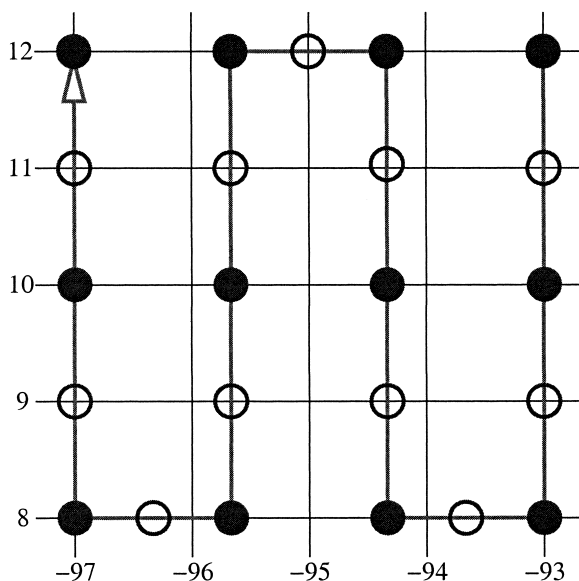


FIG. 3. Trajectory of P-3 in ITCZ study region flights. The solid circles show locations at which dropsondes were released on all flights. In addition, on some flights dropsondes were released at some or all of the locations indicated by open circles.

3. Data

Table 1 shows information about all of the research flights made by the NCAR C-130 and the NOAA P-3. The C-130 was available to the project for the period 1 September–10 October 2001. The P-3 was available 1 September–7 October, but was absent 21–27 September due to commitments to other projects. Unfortunately, the first mission after its return resulted in an engine failure on the P-3 early in the flight, which put the aircraft out of action until 3 October.

In this section we describe the treatment of the data used in this paper.

a. In situ aircraft data

On all but one flight the P-3 flew the pattern illustrated in Fig. 3 at a nominal elevation of 1900 m. The remaining flight was flown outbound and inbound along 5°N to 95°W at 1900 m. The elevation was chosen as it was optimal for the launch of expendable ocean probes. Results from these probes will be reported elsewhere.

For 95°W missions the C-130 flew a north–south trajectory along this longitude line as shown schematically in Fig. 4. The elevation of the outbound leg alternated between 30 and 1600 m as shown, while the return leg was flown at 6300 m. The C-130 flew a variety of patterns in the ITCZ missions, with many devoted to seeking out regions of developing convection and making systematic cloud penetrations at a variety of levels.

The aircraft in situ data required some rather spe-

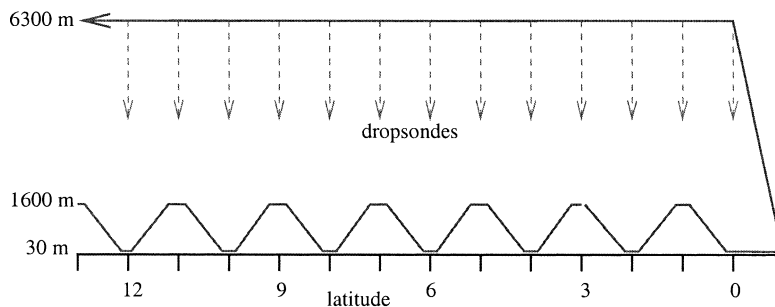


FIG. 4. Trajectory of C-130 in 95°W missions. The nominal elevations for each flight segment are shown at left. Dropsondes were launched from 6300 m every degree from the equator to 12°N on the return segment.

cialized corrections to be made. These are described in the appendix.

b. P-3 radar data

The tail radar of the P-3 aircraft (NOAA-43) was run in a dual pulse rate mode as described by Jorgensen et al. (2000), so that the Nyquist velocity was roughly 36 m s^{-1} . Only reflectivity data are used in this paper. Data were interpolated to a single $5 \text{ km} \times 5 \text{ km} \times 0.5 \text{ km}$ grid covering the region $7^\circ\text{--}13^\circ\text{N}$ and $92^\circ\text{--}98^\circ\text{W}$ from the surface to 20 km.

Rainfall rates were estimated from the radar reflectivity at $z = 1.5 \text{ km}$ using the average reflectivity–rainfall-rate relation derived from C-130 cloud penetrations during EPIC2001 (D. Baumgardner 2002, personal communication):

$$Z = 153R^{1.53}. \quad (5)$$

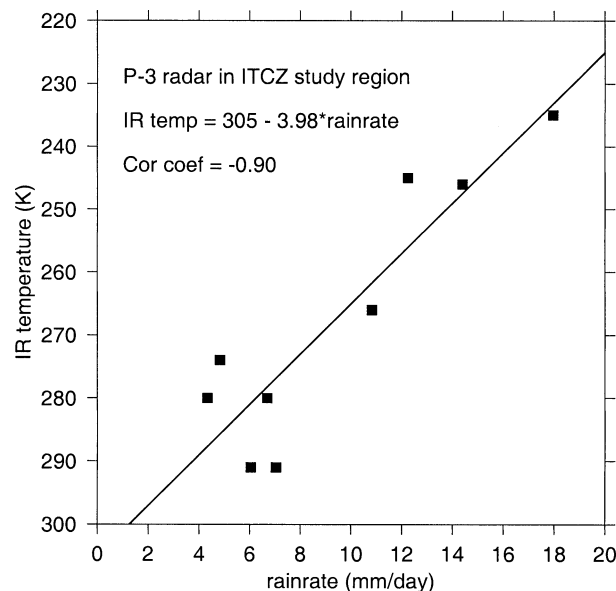


FIG. 5. Plot of rainfall rate from the P-3 radar averaged over the ITCZ study region vs the average infrared brightness temperature over this region.

This Z – R relationship does not yield results significantly different from those produced by other such relationships (e.g., Jorgensen and Willis 1982) in the literature. As with all such relationships, it cannot be expected to yield results of high accuracy. For each P-3 flight in the ITCZ study region (except mission 1, for which problems exist with the radar data), an area-averaged rainfall rate was computed over the domain $8^\circ\text{--}12^\circ\text{N}$ and $93^\circ\text{--}97^\circ\text{W}$.

Figure 5 shows a plot of area-averaged rainfall rate versus the average Geostationary Operational Environmental Satellite (GOES) infrared brightness temperature in the the ITCZ study region. The infrared brightness temperature was computed as the grand average of the average brightness temperature of a square patch 1.2° on a side centered on the P-3 as it executed its ITCZ pattern. This eliminates the effect of possible time skewing associated with the 5-h interval required to execute the pattern.

The observed correlation between radar rainfall rate and infrared brightness temperature indicates that the latter is an imperfect, but usable surrogate for the former.

c. Dropsondes

The P-3 dropped dropsondes from an elevation of 1900 m at the locations indicated by circles in Fig. 3. Every flight dropped sondes in the locations indicated by filled circles. However, some flights dropped sondes at some or all of the locations indicated by open circles. The C-130 dropped sondes every degree from the equator to 12°N as indicated in Fig. 4.

Dropsondes from the C-130 and P-3 aircraft were processed using the Aspen software package available from NCAR. This software corrects for lag effects in the temperature and humidity sensors. In addition, it inserts aircraft in situ data as the first data point in the dropsonde file. As significant corrections to aircraft in situ data were made, these data points were replaced by 10-s averages of processed aircraft data centered on the drop time of each sonde.

Dropsonde signals are often intermittent. Furthermore, the Aspen program omits temperature and hu-

midity data from dropsondes for roughly the first 20 and 60 mb, respectively, because the sensors are adjusting to the environment during this interval. Linear interpolation to a 5-mb grid was therefore done between levels exhibiting good data, including the initial aircraft data. All soundings were visually inspected for excessively large data gaps or obviously erroneous data, and discarded if these flaws occurred.

P-3 dropsondes deployed on the periphery of the ITCZ study region were used to compute the net lateral mass flux in or out of this region. From this the mean vertical velocity at 1900 m in the study region was obtained. The mean horizontal wind measured by a dropsonde is simply the difference in initial and final horizontal positions divided by the drop duration. The error in this difference is surely less than 100 m, given the accuracy of GPS positioning. For a drop time of 5 min, this implies an error in the vertically averaged wind of less than 0.3 m s^{-1} . Between 10 and 14 dropsondes were deployed on the periphery of this region for each flight, which implies a further factor of 3 or 4 reduction in random fractional error when integrated over all of the dropsondes. Thus a mean instrumental error of less than 0.1 m s^{-1} can be expected in the mean normal velocity component measured by the dropsondes. This translates into an instrumental error of less than 0.002 m s^{-1} in the mean vertical velocity at 1900 m obtained from mass continuity.

Sampling errors due to sparse coverage of the periphery of the ITCZ study region by dropsondes and to time aliasing are harder to evaluate. The flights with 14 dropsondes on the periphery of the study region had dropsonde spacings of 1° on the east and west sides and 1.33° on the north and south sides. Reduction of the dropsonde sampling interval from 1° to 2° on the east and west sides of the ITCZ study region resulted in changes in the vertically averaged mass divergence of 10% to 15%, which is small compared to other potential errors. This suggests that sampling of the winds on the periphery of the ITCZ dropsonde region was generally adequate.

The infrared brightness temperature averaged over the ITCZ study region ought to have the same time variability as the divergence averaged over this region, since the divergent convective flows are physically related to the cloudiness. Figure 6 shows a plot of the lagged autocorrelation function of the region-averaged brightness temperature. For a lag of 5 h (the approximate time needed by the P-3 to complete deployment of the dropsondes), the correlation is ≈ 0.8 , which suggests that major changes in the domain-averaged divergence typically did not occur during the dropsonde deployment period. From these arguments we conclude that the domain-average vertical velocity at 1900 m inferred from the dropsondes is typically within 20% to 30% of its actual mean value over the 5-h sample period.

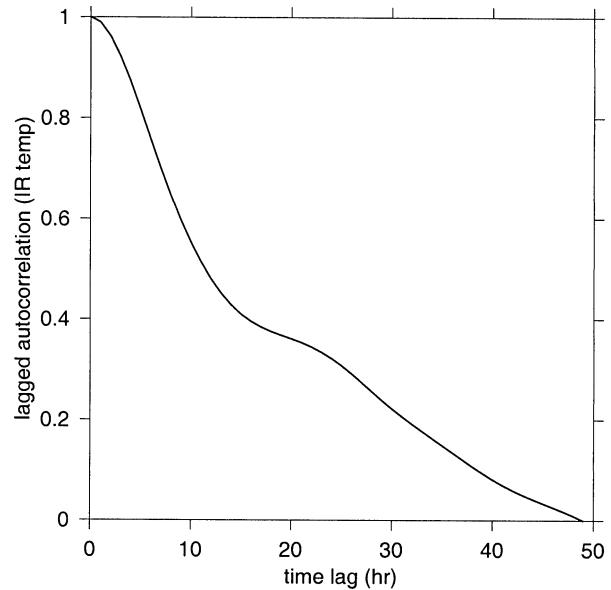


FIG. 6. Lagged autocorrelation function over the period of the field program for the satellite infrared brightness temperature averaged over the $4^\circ \times 4^\circ$ ITCZ study region.

d. Ship sounding data

The ship *Ron Brown* launched radiosondes 6 times a day from near 10°N , 95°W during the period 12 September–1 October 2001. Sounding data were treated similarly to dropsonde data.

e. GOES satellite data

Hourly GOES satellite infrared and water vapor imagery were collected from the University Corporation for Atmospheric Research (UCAR) Unidata Internet data distribution network. Data were interpolated to a 0.2° grid over the experimental area. Interpolation was done linearly across missing images caused by network or satellite outages, resulting in a continuous interpolated record for the entire project.

f. Entropy calculation

The formula used for entropy is

$$s = (C_{pd} + C_t q_t) \ln(T/T_R) - R_d \ln(p_d/p_R) - q_v R_v \ln(q_v/q_s) + L(T)q_v/T, \quad (6)$$

where C_{pd} and R_d are the specific heat at constant pressure and the gas constant for dry air, R_v is the gas constant for water vapor, $L(T)$ is the temperature-dependent latent heat of vaporization, T is the absolute temperature, p_d is the partial pressure of dry air, q_v is the water vapor mixing ratio, q_s is the saturation mixing ratio, q_t is q_v plus the mixing ratio of condensed water, and $T_R = 273.15 \text{ K}$ and $p_R = 10^5 \text{ Pa}$ are constants (Emanuel 1994). The liquid water content is ignored in the present

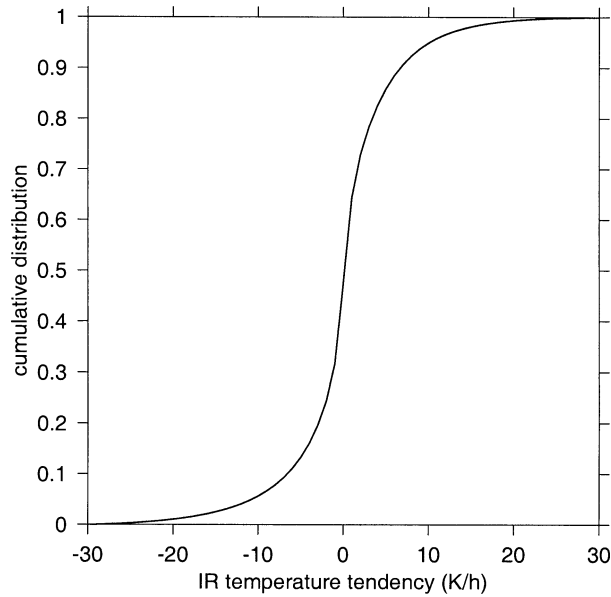


FIG. 7. Cumulative distribution of infrared brightness temperature tendencies over the ITCZ study region during the EPIC2001 field program.

work, as the resulting error is generally minor. This formula also neglects the ice phase, which is not a significant problem, as most of our measurements are below the freezing level. The saturated specific moist entropy s_s is obtained by setting $q_v = q_s$ in the above equation.

Sounding plots are made by plotting the entropy and saturated entropy as a function of pressure. The interpretation of these plots is qualitatively identical to that of commonly made plots of equivalent potential temperature and saturated equivalent potential temperature versus pressure.

In order to make comparisons with standard meteorological variables, the following approximate equivalences are given.

- A temperature or equivalent potential temperature change of 1 K changes the entropy by about $3 \text{ J kg}^{-1} \text{ K}^{-1}$.
- A water vapor mixing ratio change of 1 g kg^{-1} changes the entropy by about $8 \text{ J kg}^{-1} \text{ K}^{-1}$.
- The variation of potential temperature with pressure and saturated moist entropy is complex, but is shown by the curved lines slanting to the left in soundings such as given in Fig. 8, which represent contours of potential temperature at 5-K intervals.

4. Direct forcing of convection

As indicated in section 2, convection is generally thought to occur when conditional instability is realized. Numerous dropsondes were deployed during EPIC2001 in all kinds of conditions. We use soundings within the

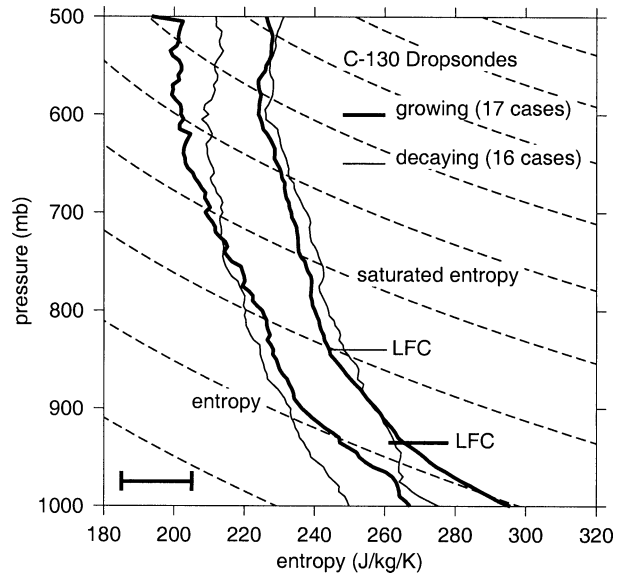


FIG. 8. C-130 dropsonde soundings expressed as plots of (left) entropy and (right) saturated entropy vs pressure. The thick lines represent the average of soundings for which the satellite infrared brightness temperature is decreasing by more than 4 K h^{-1} , whereas the thin lines are an average for which the brightness temperature is increasing by more than this rate. The LFC of surface parcels are indicated for the two cases. The dashed lines represent contours of constant potential temperature at 5-K intervals. Note that the entropy is conserved in ascent and descent by both saturated and unsaturated parcels, whereas the saturated entropy of an unsaturated parcel is not conserved, but moves along a potential temperature contour in ascent and descent. The error bar in the lower left corner shows the typical standard deviation of both the entropy and the saturated entropy at each level.

ITCZ study region in conjunction with hourly GOES infrared satellite observations to identify conditions favorable to the local development of convection, that is, on scales smaller than 50 km. We find from direct observation that regions with rapidly decreasing brightness temperatures are correlated with deep convective development, whereas regions with increasing temperatures identify decaying convection.

Figure 7 shows the cumulative distribution of satellite infrared brightness temperature tendencies averaged over pixels of size $0.1^\circ \times 0.1^\circ$ in the ITCZ study region during the EPIC2001 field program. The time derivative of brightness temperature is derived applying centered differences to the hourly infrared temperature data. Only 17% of pixels have tendencies less than -4 K h^{-1} , while 6% of pixels have tendencies less than -10 K h^{-1} . Thus, regions of rapidly decreasing brightness temperature are relatively sparse. Nevertheless, the incidence of such regions tends slightly to lead the development of low average infrared brightness temperature over the entire $4^\circ \times 4^\circ$ ITCZ study region, suggesting that small areas of rapidly decreasing brightness temperatures are related to the initiation of broader convective outbreaks.

Figure 8 shows the averages of soundings with nearby infrared brightness temperature tendencies $< -4 \text{ K h}^{-1}$

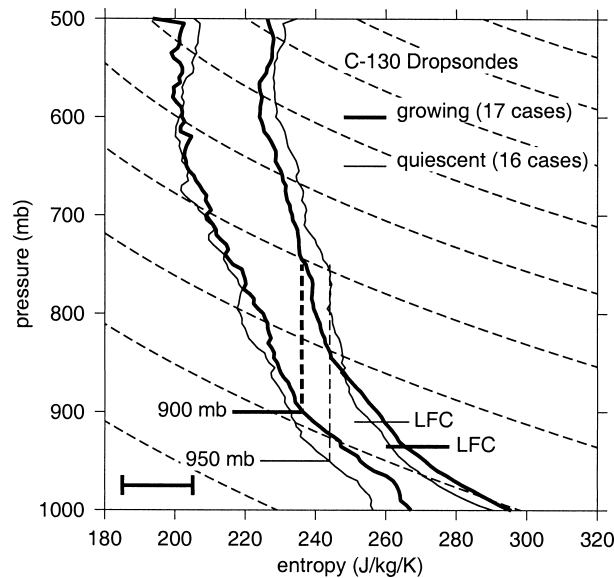


FIG. 9. As in Fig. 8, except soundings in convectively developing (thick lines) and quiescent regions (thin lines). The vertical dashed lines show the origins of lifted parcels in each case, which would be neutrally buoyant at 750 mb.

(heavy lines) and $>4 \text{ K h}^{-1}$ (thin lines). The brightness temperature near a dropsonde site is obtained by averaging hourly GOES data over a 0.4° (45 km) square centered on the dropsonde location. As expected, developing convective regions are more moist and unstable at low levels than decaying regions, with respective LFCs for surface parcels of 940 and 830 mb for the two cases. (Virtual temperature effects have not been included in the computation of these LFCs, as these produce nearly constant biases which do not significantly affect our arguments.) Interestingly, the entropy above about 700 mb in decaying regions is higher than that of developing regions, suggesting that a recent history of strong convection is responsible for moistening these levels.

One word of caution: the sample for developing convection is only 17 soundings and drops from 17 to 13 above 620 mb, as four of the dropsondes in this sample were deployed from near this altitude. However, all sample members were available through the entire displayed depth for the decaying convective regions.

The stabilization of the low-level environment under decaying convection is a well-known phenomenon explored first in tropical oceanic regions by Zipser (1969, 1977), and is due to the displacement of unstable boundary layer air by stable air from convective and mesoscale downdrafts. The boundary layer is known to recover from this stabilization over a period of 12–24 h via the action of surface heat (or entropy) fluxes. Figure 8 represents the extremes of this boundary layer depletion–recharge cycle.

The lack of deep convection in downdraft-stabilized regions is no mystery. Less clear are the reasons why

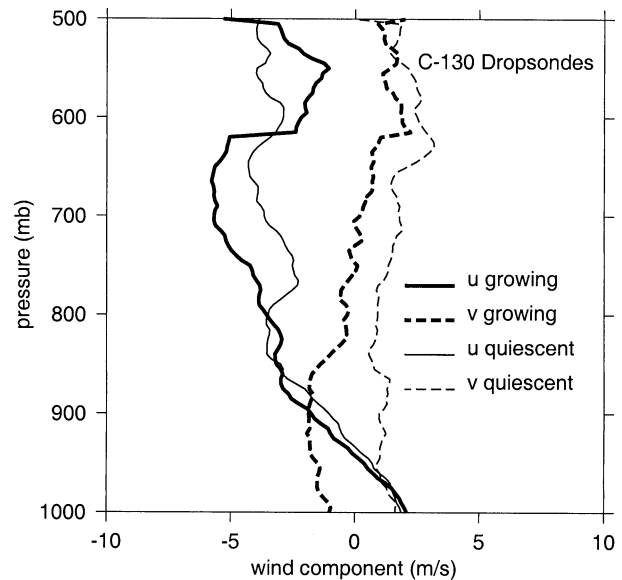


FIG. 10. Wind profiles corresponding to the thermodynamic profiles shown in Fig. 9. Convectively developing cases are shown by thick lines and quiescent regions by thin lines.

quiescent regions containing shallow cumulus clouds do not immediately develop, since often CAPE is ample and CIN is small in these regions. Figure 9 compares the convectively developing environment of Fig. 8 with quiescent regions, which contain at most only nondeveloping small convection. This is ensured by limiting consideration to regions with a temperature tendency between -2 and $+2 \text{ K h}^{-1}$ and by setting a lower limit of 280 K on the brightness temperature itself.

In comparison with the convectively developing regions, the quiescent regions have somewhat lower entropy values below 900 mb and slightly lower saturated entropy below 850 mb. Also, the well-mixed surface layer of entropy is thinner in the quiescent case. The LFC is correspondingly higher, being near 910 mb, as opposed to 940 mb for regions with rapidly decreasing brightness temperature. Above 850 mb the entropy profiles of the two cases are essentially identical, but the saturated entropy is slightly higher in the quiescent case, reflecting a slightly warmer free troposphere. These results are quite similar to those obtained by Kingsmill and Houze (1999a,b) for the western equatorial Pacific, with the exception that we do not see a significant difference in the moisture (as represented by the entropy) between the quiescent and developing cases above 850 mb.

Figure 10 shows the wind profiles in the convectively developing and quiescent cases illustrated in Fig. 9. No significant difference in wind shear exists between the two cases. However, the developing situations tend to have a slightly more northerly wind component.

The averaging performed in Figs. 8–10 hides variability that helps to explain why convection developed or not in particular situations. The error bars in Figs. 8

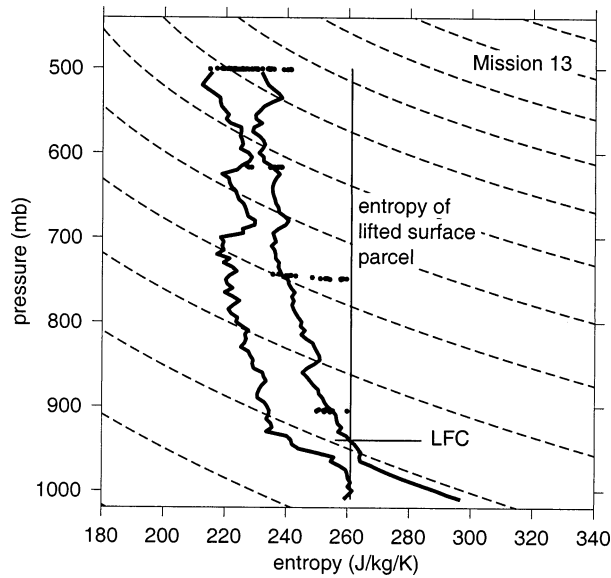


FIG. 11. Proximity sounding showing entropy and saturated entropy profiles in inflow region for a weak convective line near 12°N , 95°W on 29 Sep 2001 (mission 13; day 272). The dots show 1-s samples of the in-cloud entropy (cloud water density $> 0.05 \text{ g m}^{-3}$, updraft $> 1 \text{ m s}^{-1}$) measured during C-130 penetrations at various levels.

and 9 show approximate one standard deviation limits for both the entropy and the saturated entropy. To further bring out this variability, we show in Figs. 11–15 environmental soundings and in-cloud entropies for five cases in which the C-130 made cloud penetrations. (In-cloud temperatures used to compute entropies inside of cloud are obtained using a radiometric thermometer; see the appendix for a discussion of this instrument.)

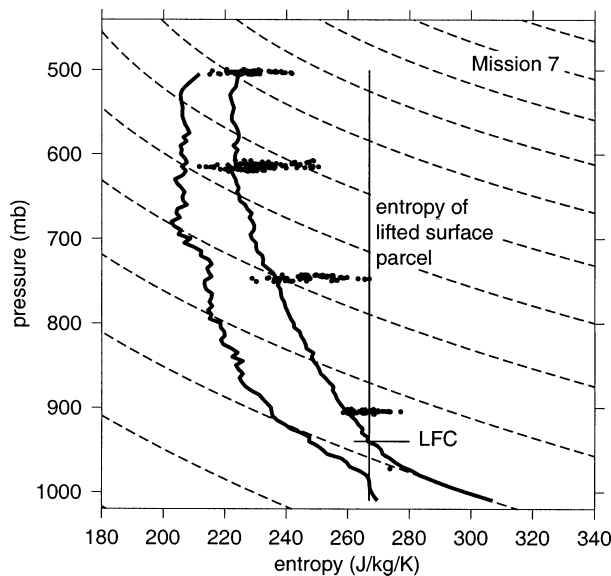


FIG. 12. As in Fig. 11, except for a region of growing convective cells in low shear near 11.5°N , 95°W on 16 Sep 2001 (mission 7; day 259).

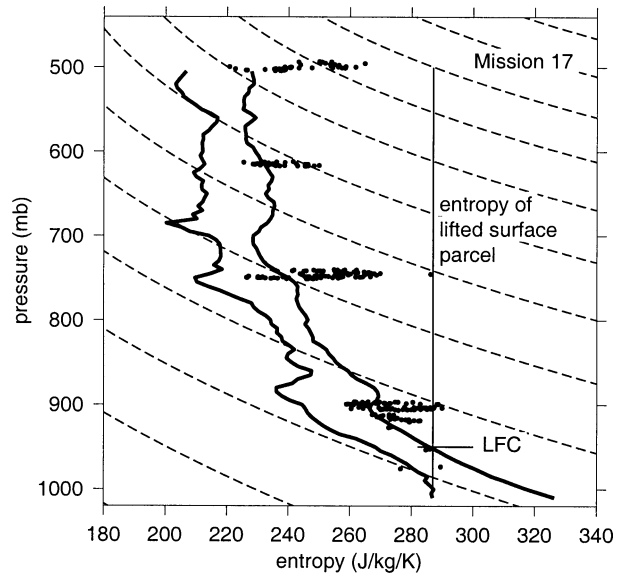


FIG. 13. As in Fig. 11, except for a region of vigorous growing convection in easterly shear near 12°N , 94°W on 6 Oct 2001 (mission 17; day 279).

Figure 11 shows a borderline case in which infrared brightness temperatures in the region studied were generally warming. Nevertheless, active deep convection was still in progress in the convective line observed, though it was visibly weakening during the study.

Figures 12 and 13 show soundings and in-cloud data associated with vigorous convection occurring in regions of rapidly decreasing infrared brightness temperature. The case shown in Fig. 13 had the strongest updrafts observed during EPIC2001.

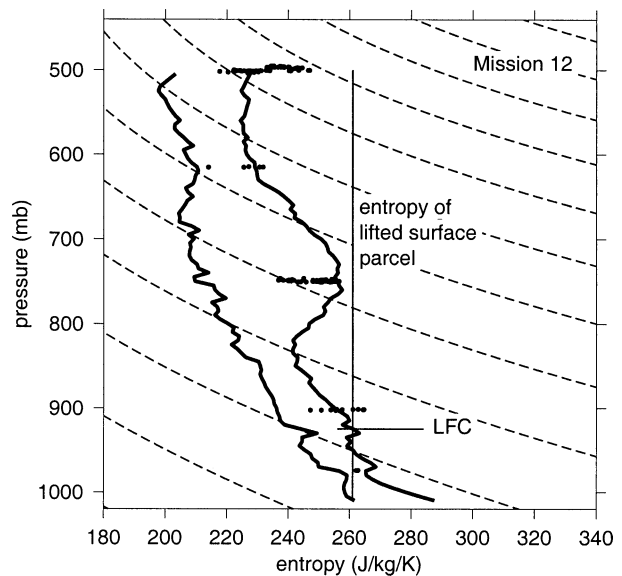


FIG. 14. As in Fig. 11, except for a region of very weak convection reaching the middle troposphere near 9°N , 94°W on 28 Sep 2001 (mission 12; day 271).

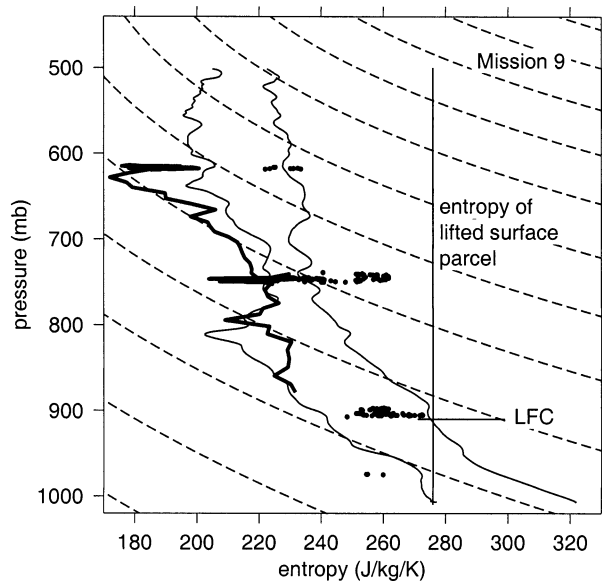


FIG. 15. As in Fig. 11, except for a region of convection capped by a dry layer near 11°N, 96.5°W on 20 Sep 2001 (mission 9; day 263). The thin lines represent an aircraft sounding taken a few tens of kilometers north of the convection. The thick line is the entropy in the immediate vicinity of the convection.

Figure 14 shows a sounding in which convection was strongly inhibited by an inversion near 750 mb. Occasional convective cells were ascending to the middle troposphere and perhaps above, but they were sparse and short-lived. Infrared brightness temperatures were increasing in this region.

Figure 15 shows a case in which dry, midtropospheric air in the immediate vicinity of the convection succeeded in inhibiting development above 600 mb, even though the updrafts at 750 mb were as strong as those in the case shown in Fig. 12. These observations were taken at the east end of an east–west line in a region of easterly shear. Further west in the line the convection was much deeper. This is probably a case in which “sacrificial clouds” rapidly moistened the impinging dry air from the east, allowing clouds further west along the line to ascend through this dry layer.

A common theme of all of the above cases is that deep convective updrafts reaching 750 mb contain a broad range of entropies characteristic of the environmental air originating from near the surface to at least 900 mb. Thus, the buoyancy of updrafts is in general much less than might be expected from normal CAPE calculations, which lift a parcel conservatively from the somewhat thinner subcloud layer.

One can imagine a number of scenarios leading to the observed distribution of incloud entropy. For instance, plumes originating near the surface might entrain enough in their ascent to generate the observed dilution of surface parcels. Alternatively, the entire ≈ 100 -mb-thick conditionally unstable layer may contrive by some mechanism to produce ascending parcels, which become

the updrafts of deep convection. The details of this process are unknown at this point, but the constitution of deep convective updrafts seems beyond dispute.

Figure 9 shows that in the case of developing systems, environmental parcels from as high as 900 mb become positively buoyant above 750 mb, whereas the corresponding upper limit for the quiescent case is 950 mb. Except for the fact that we have observations at this level as a target LFC. However, the general conclusion that unstable air is confined to a thinner layer in the quiescent case compared to the developing case is independent of our choice of target LFC. For any reasonable choice, the thickness of the layer available for deep convective ascent is much less in the quiescent case than in the developing case, even though lifted surface parcels in the quiescent case become buoyant on the average above 910 mb.

In order to explain the above results, we hypothesize that deep convection over tropical oceans needs a deep, conditionally unstable layer, that is, a deep layer from which lifted parcels eventually reach a level of free convection, from which to develop. We explore the consequences of this hypothesis below.

Let us define an index of deep convective inhibition (DCIN) for a heterogeneous parcel originating from a deep layer, which is lifted above the tops of shallow convective clouds, which are typically near 850 mb:

$$\text{DCIN} \equiv s_t - s_b, \quad (7)$$

where s_t is the threshold entropy, taken to be equal to the mean saturated entropy in the 810–830-mb layer, and s_b is the average entropy in the 900–1000-mb layer. (The rather thin layer chosen to represent s_t is dictated by the typical launch altitude for the P-3 dropsondes of ≈ 812 mb).

DCIN computed from C-130 dropsondes is correlated with the satellite-observed infrared brightness temperature tendency. This is shown in Fig. 16, which presents a scatterplot of infrared temperature tendency versus DCIN for all C-130 dropsondes deployed in the ITCZ study region. The correlation is not particularly strong, with a correlation coefficient of only 0.43. However, the correlation is significant at the 99% level, so the relationship is robust, though noisy.

The C-130 dropsonde dataset is unique in that the C-130 visually sought out the rare instances of developing convection in otherwise clear regions during ITCZ missions, thus biasing the sample toward these regions. The P-3 dropsondes and ship *Ron Brown* radiosonde soundings were not biased in this way, but nevertheless exhibit correlation coefficients of order 0.25, significant at the 95% level (plots not shown).

A more conventionally defined convective inhibition index also shows correlation with infrared brightness temperature tendency. Such an index is obtained by defining the threshold entropy s_t in (7) to be the average saturated entropy in the range 900–950 mb and the par-

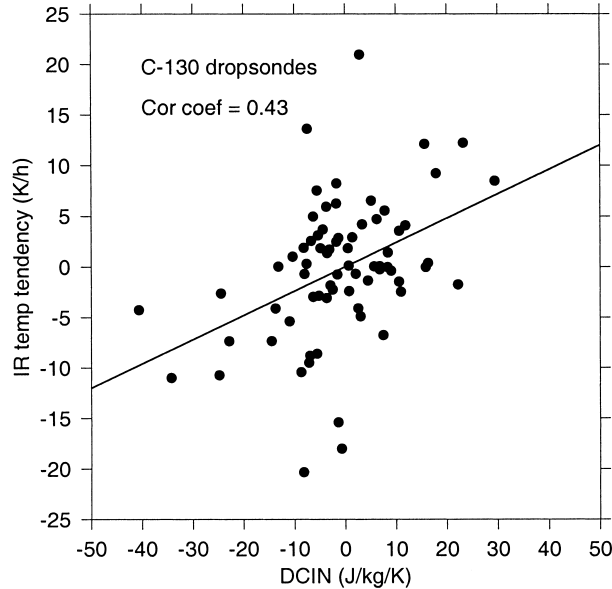


FIG. 16. Scatterplot of DCIN for C-130 dropsondes in the ITCZ study region vs infrared brightness temperature tendency in a $0.4^\circ \times 0.4^\circ$ box centered on each dropsonde.

cel entropy s_b to be the average entropy in the range 970–1000 mb. However, in all three of the above sets of soundings, the correlation with brightness temperature tendency is slightly weaker than that for DCIN.

5. Environmental control of DCIN

In this section we shift from a consideration of convective forcing at a point to the development of a model of convective forcing averaged over a region several hundred kilometers in extent. In order to make sense of this, we need to work with the distribution of DCIN rather than its value at a particular point. Furthermore, since even a convectively active region exhibits mostly stable values of DCIN, the unstable tail of the DCIN distribution must particularly be considered.

Evidence from observations presented in the previous section suggests the following.

- 1) Deep convection is initiated in those rare locations where the deep convective inhibition is sufficiently negative. High values of deep boundary layer entropy s_b and slightly cooler than average temperatures above 850 mb, leading to a lower convective threshold entropy s_t , are about equally responsible for these negative values in our sample of C-130 soundings.
- 2) Negligible difference in wind shear profiles exists between regions of developing deep convection and nondeveloping regions, suggesting that variations in wind profiles exert little or no control over the initiation of deep convection in our sample.
- 3) Little difference is found in the entropy (and hence absolute humidity) profiles above 850 mb between developing and nondeveloping cases.

In summary, negative values of DCIN appear to correlate with deep convective development in our sample. This correlation is robust even though it is noisy. We therefore focus on the processes that control the boundary layer entropy s_b and the threshold entropy s_t , which enter the definition of DCIN (7).

a. Boundary layer entropy balance

The in situ and dropsonde measurements made by the P-3 aircraft allow us to estimate the terms in the entropy budget using (3) applied to a control volume bounded below by the ocean surface, above by the 812-mb (≈ 1900 m) P-3 flight level, and laterally by the periphery of the $4^\circ \times 4^\circ$ ITCZ study region. The surface entropy flux is estimated using a bulk flux formula applied to boundary layer and surface conditions inferred for each P-3 dropsonde in the ITCZ study region:

$$F_{es} = \rho_b C_D U_b (s_{ss} - s_b), \quad (8)$$

where ρ_b is the boundary layer air density, the exchange coefficient is $C_D = 0.0011$, U_b is the wind speed in the boundary layer (taken here to be the mean value in the 980–1000-mb layer), s_{ss} is the saturated entropy at the temperature and pressure of the sea surface, and s_b is the boundary layer entropy. The resulting values are then averaged over all dropsondes. Lateral fluxes are obtained from dropsondes deployed on the boundary of the ITCZ study region. From three to five sondes were deployed on each side of the 4° square. Entropy fluxes through the top of the control volume were estimated from in situ P-3 data. Direct radiative effects were estimated assuming a mean radiative cooling rate of 1.5 K day^{-1} within the control volume. All contributions to the budget were expressed as partial mean entropy tendencies within the control volume. Table 2 shows the partial tendencies from each of these sources as well as their sum, labeled as the residual.

Also shown in Table 2 are the area-averaged rainfall rate as provided by the P-3 radar, and the mean vertical velocity through the top of the control volume, estimated from mass continuity using the dropsonde measurements. Note that the lateral and top fluxes are, strictly speaking, not eddy fluxes, as the mean values of the normal velocity on the lateral faces and the vertical velocity on the top face have not been subtracted before multiplying by s' and averaging. In order to ensure consistency, a small constant is added to the aircraft vertical wind speeds at the top of the volume in order to make the mean value of this quantity match the mean vertical velocity inferred from the dropsonde measurements using mass continuity.

The reference entropy is defined as the updraft-weighted mean entropy from the P-3 in situ measurements:

$$s_R = \overline{w_u s / w_u}, \quad (9)$$

where w_u equals the vertical wind w for $w > 0$ and is

TABLE 2. Entropy budget for ITCZ region below 1900-m elevation from P-3 ITCZ missions. “Wmean” is the mean vertical velocity (m s^{-1}) at 1900 m. The budget contributions “Surf,” “Lat,” “Top,” and “Rad” represent the partial tendencies of entropy in the box ($\text{J kg}^{-1} \text{K}^{-1} \text{day}^{-1}$) due to surface entropy flux, lateral entropy influx, influx through the top (at 1900 m), and radiation. “Resid” is the sum of the partial tendencies, and “Ctop” is “Top” with fluxes due to vertical velocities less than 1 m s^{-1} in magnitude suppressed. “Rain” indicates the radar-derived rainfall rate (mm day^{-1}).

Mission	Wmean	Surf	Lat	Top	Ctop	Rad	Resid	Rain
1	0.020	15.3	6.3	-24.6	-22.4	-5.0	-8.0	—
2	0.013	21.1	4.1	-0.1	-5.1	-5.0	20.1	6.7
4	0.018	30.7	9.8	-41.4	-24.9	-5.0	-5.9	18.0
5	0.010	12.9	7.1	-10.6	-6.2	-5.0	4.4	7.0
7	-0.001	20.2	3.0	-19.4	-12.0	-5.0	-1.2	14.4
9	0.004	18.1	9.1	-7.5	-7.4	-5.0	14.7	10.8
15	0.001	16.2	8.6	-0.7	-2.0	-5.0	19.1	6.0
16	0.013	11.6	9.1	-34.7	-25.1	-5.0	-19.0	4.3
17	0.012	18.8	12.8	-19.6	-19.5	-5.0	7.0	12.2
18	0.007	15.1	5.5	-5.9	-7.2	-5.0	9.7	4.8

set to zero for $w < 0$. With this definition of s_R , updrafts contribute nothing to the entropy budget, and w_s' at the top of the control volume is attributable entirely to downdrafts.

Vertical air motions above the boundary layer are generally due either to passing gravity waves or to moist convective updrafts and downdrafts. The former typically have magnitudes less than 1 m s^{-1} and should not transport entropy due to their cyclic vertical displacement. However, the clear regions subject to gravity wave fluxes generally cover the vast majority of the domain near 812 mb, with convective updrafts and downdrafts existing in only a tiny part of the domain. Thus, accumulated small systematic errors of cancellation in the wave transport as well as the weak bulk transport due to the mean vertical motion could, in principle, dominate the convective transport of entropy through the top of the control volume. As a test of this, vertical velocities less than 1 m s^{-1} in magnitude were set to zero in an alternate calculation of fluxes at the top of the domain. This calculation should eliminate the majority of the wave and weak mean transport, leaving only the moist convective part. As Table 2 shows, this omission results in relatively small changes in the volume-top fluxes in most cases, which means that convective transports tend to dominate the entropy flux through the top of the control volume.

The residuals to the entropy budget computed in Table 2 can be attributed either to actual entropy tendencies in the control volume or to errors in computing one or more of the partial tendencies. We cannot rule out the former possibility, though residual values are typically twice the entropy tendencies seen in the lowest 200 mb from *Ron Brown* soundings with a half-day low-pass filter applied. However, there is ample reason to believe that most of the terms in the entropy balance have large potential errors. The greatest errors are probably due to the undersampling of volume-top conditions by in situ observations. The P-3 track was about 2200 km in length, which was long enough to capture numerous

clouds, but perhaps not a statistically stable sample of them.

In light of these issues, it would be unwise to take the residuals and the actual values of partial contributions too quantitatively. However, we argue that the values presented can be considered typical of conditions in this region. Given this caveat, we can still draw a number of conclusions from these results.

- 1) The two largest contributors to the entropy budget in the selected control volume are the surface fluxes and the volume-top downdraft fluxes.
- 2) To the extent that our assumption regarding the radiative cooling rate is valid, the direct radiative loss of entropy in the control volume is minor.
- 3) The contribution of the lateral flux of entropy is always positive, but is typically a half or a third of that due to surface fluxes. The absence of strongly negative values indicates that the strong influx of dry air frequently seen in the equatorial western Pacific (Yoneyama and Parsons 1999) must be less common in the eastern Pacific.
- 4) The mean vertical velocity at 1900 m is positive in all but one case. This ascent is associated with the consistent termination of the low-level cross-equatorial southerly flow within the bounds of the ITCZ study region. Interestingly, the correlation between the mean vertical velocity at 1900 m and the radar-measured rainfall rate is insignificant, with a correlation coefficient of 0.13.
- 5) A cursory examination of Table 2 shows that the strengths of downdraft fluxes are related fairly closely to the rainfall over the control volume in most cases, which suggests that the in situ sampling of fluxes by the P-3 was not too unrepresentative (correlation coefficient: 0.53).
- 6) The correlation between surface fluxes and rainfall rate is even higher (correlation coefficient: 0.83, significant at the 95% level). Thus, in a sample of nine P-3 flights for which we have complete data, the variations in the surface entropy flux averaged over

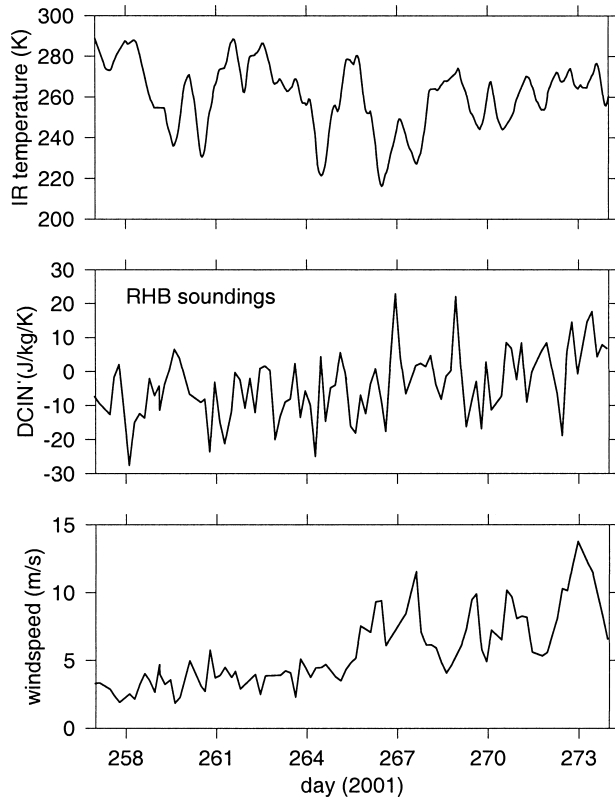


FIG. 17. (top) Satellite infrared brightness temperature over the ITCZ study region, (middle) DCIN and (bottom) wind speed averaged over the lowest 100 mb for 17 days of ship *Ron Brown* radiosonde soundings taken near 10°N , 95°W .

the ITCZ study region account for 2/3 of the variance in mean rainfall rate in that region.

The above results suggest that the primary balance in the entropy budget in the ITCZ study region is between surface fluxes and the import of low entropy air into the boundary layer by downdrafts, as postulated in the theory of boundary layer quasi equilibrium (Raymond 1995). Furthermore, rainfall is highly correlated with surface entropy fluxes. Lateral import of entropy (i.e., via advection, as discussed in section 2) is of lesser importance in our sample. Shallow ascent forced by the SST distribution (or possibly by some other mechanism such as Ekman pumping) appears to have little directly to do with the production of rainfall and the development of deep convection in this region, at least in our sample.

b. Variations in threshold entropy

Variations in the saturated entropy profile (and hence the temperature profile) are almost certainly due to adiabatic ascent or descent forced by some dynamical mechanism. The threshold entropy in the definition of DCIN is affected by these vertical motions.

The six daily soundings from the ship *Ron Brown* enable us to study time variations in the boundary layer

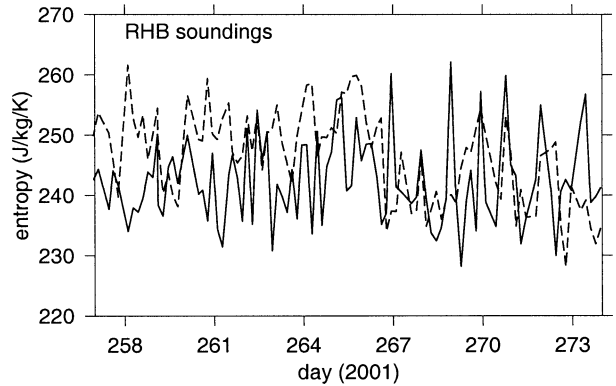


FIG. 18. Threshold entropy s , (saturated entropy averaged over 810–830 mb; solid line) and boundary layer entropy s_b (entropy averaged over 900–1000 mb; dashed line) for *Ron Brown* soundings as shown in Fig. 17.

and threshold entropies for an extended period. Figure 17 shows the fluctuations in DCIN in *Ron Brown* soundings over 17 days when the *Brown* was located near 10°N , 95°W . Also seen is the wind speed averaged over the lowest 100 mb of the sounding. DCIN exhibits strong short-term fluctuations, but these are superimposed on a longer-term trend, which follows the observed trend in the wind speed. The wind also fluctuates, but on average increases from about 2 to 8 m s^{-1} over the 17-day period. This is accompanied by an increase in DCIN (i.e., decreasing instability) from about $-10\text{ J kg}^{-1}\text{ K}^{-1}$ to near zero. The infrared brightness temperature is a minimum during the middle of the period, when the wind speed has increased somewhat from its initial value, but the value of DCIN has not. Thus, the strongest convection appears to require both higher wind speeds and lower DCIN values.

Figure 18 shows the individual fluctuations in the boundary layer and threshold entropies. The long-term trend in DCIN clearly comes from variations in the boundary layer entropy. The threshold entropy is subject to strong short-term fluctuations, but exhibits much smaller long-term variability than the boundary layer entropy. However, the fluctuations in the threshold entropy are as large as those in the boundary layer entropy.

There are two plausible origins for free tropospheric vertical motions in the tropical eastern Pacific. Either the vertical motion is associated with large-scale wave or quasibalanced forcing, as noted in section 2, or it is the result of small-scale gravity waves or cold pool dynamics, possibly produced by other nearby convection (Mapes 1993). In the former case, one would expect to see perturbations in the saturated entropy profile that are similar over a broad area, whereas more local variability in the profile would be found in the latter case.

The origin and scale of the fluctuations in threshold entropy are unknown at this point. However, the spatial scale can be large enough to suppress deep convection over the majority of the ITCZ study region, the con-

ditions during mission 2 being a case in point. Thus, as Kloesel and Albrecht (1989) noted, large threshold entropy, manifested as an inversion layer in their analysis, can act to suppress the development of deep convection.

c. Convective forcing function

From the above work, we conclude that strong surface entropy fluxes and the existence of sufficiently negative values of DCIN somewhere in a specified region are potential predictors of deep convection and precipitation. The average value of DCIN over a region a few degrees in diameter is only weakly correlated with the presence in that region of values low enough to initiate convection. This is because convectively active regions have broader DCIN distributions than inactive regions, due to the existence of cold pools resulting from previous convection (Raymond 1995; Kingsmill and Houze 1999b). Therefore, a convectively active region may actually have higher mean DCIN than an inactive region, even though the low end of the distribution might be lower. Thus, we need a better indicator of the existence of strongly negative DCIN (i.e., weak convective inhibition) *somewhere* over the ITCZ study region. Lacking comprehensive information about the distribution of DCIN on many of the days, we define a surrogate for typical DCIN values in the unstable tail of the distribution as

$$\text{DCINLOW} = \text{av}(\text{DCIN}) - 2 \times \text{sd}(\text{DCIN}), \quad (10)$$

where $\text{av}(\text{DCIN})$ is the average value, and $\text{sd}(\text{DCIN})$ is the standard deviation of the DCIN distribution measured from all the dropsondes deployed in the study region on a particular day. The estimate of average and standard deviation is possible with a much smaller set of soundings than is needed to sample directly the unstable tail of the DCIN distribution. Of course, the use of this indicator assumes that the shape of the DCIN distribution does not vary much from day to day.

We hypothesize that the mean infrared brightness temperature near each dropsonde, averaged over all dropsondes deployed on a particular day, can be predicted by a linear combination of the average surface entropy flux F_{es} and the value of DCINLOW for that day. This hypothesis is based on the inferred importance of surface fluxes in the control of convection once sufficiently negative values of DCIN exist, but recognizes the possibility that other effects such as large-scale subsidence may increase DCIN values to the point where surface fluxes are unable to destabilize the atmosphere.

A linear regression on all 20 missions, using P-3 dropsondes if available and C-130 dropsondes otherwise, yields a predicted infrared brightness temperature (in kelvins)

$$T_{\text{IR}} = 310 - 71.4F_{\text{es}} + 0.76\text{DCINLOW} \quad (11)$$

with a correlation coefficient of 0.82 and significance at the 99% level. The correlation coefficient between F_{es} and T_{IR} alone is 0.66, which is considerably less than the correlation between rainfall and surface fluxes for

TABLE 3. Mission-average conditions: U_b is boundary layer wind (m s^{-1}); F_{es} is surface entropy flux ($\text{J K}^{-1} \text{m}^{-2} \text{s}^{-1}$); for DCIN and DCINLOW, see text ($\text{J kg}^{-1} \text{K}^{-1}$); Obs T_{IR} and Pred T_{IR} are observed and predicted infrared brightness temperature (K), respectively.

Mission	U_b	F_{es}	DCIN	DCINLOW	Obs T_{IR}	Pred T_{IR}
1	4.8	0.376	2.2	-33.6	267	257
2	5.0	0.469	5.7	-6.6	279	271
3	7.2	0.528	-5.3	-18.8	262	257
4	6.7	0.701	10.8	-23.0	236	242
5	3.3	0.282	3.5	-20.3	291	274
6	2.2	0.188	3.4	-10.8	278	288
7	4.9	0.460	9.5	-17.4	245	263
8	4.7	0.360	2.4	-13.2	273	274
9	6.0	0.427	-1.2	-20.7	264	263
10	8.0	0.775	9.7	-18.4	234	240
11	5.5	0.461	10.8	-4.5	268	273
12	4.2	0.321	-5.2	-11.5	271	278
13	8.4	0.755	1.9	-8.6	264	249
14	1.9	0.123	-13.2	-23.3	290	283
15	4.5	0.386	8.9	-3.2	291	279
16	3.6	0.273	7.1	-9.6	277	283
17	5.0	0.437	7.5	-26.2	249	258
18	4.6	0.361	4.4	-9.8	270	276
19	2.6	0.183	-3.2	-48.9	258	259
20	4.9	0.363	-6.8	-28.5	262	262

the P-3 flights alone. This probably reflects the fact that the P-3 sample is not completely representative of conditions in the ITCZ region, and that the C-130 sample adds some qualitatively different cases. As an example, the case of mission 11 on 25 September exhibited relatively strong surface fluxes, but was convectively suppressed due to high DCIN values. The correlation coefficient between DCINLOW and T_{IR} is 0.34, significant at the 80% level (see Table 3).

The surface entropy flux and DCINLOW thus jointly account for about 2/3 of the variance in infrared brightness temperature. A plot of observed versus predicted T_{IR} is shown in Fig. 19.

We emphasize the importance of averaging over a wide distribution of soundings on each day—the strongest surface fluxes and the most negative values of DCIN generally do not coincide with the lowest values of infrared brightness temperature. Thus, surface fluxes and DCIN on one hand, and infrared brightness temperature on the other, are not well correlated on a point-by-point basis. Only when averaging is done over the full range of convective conditions existing on each day, including inflow, convectively active, and decaying regions, does the correlation emerge.

It is interesting that such a large fraction of the variance in infrared brightness temperature can be accounted for by conditions in and slightly above the atmospheric boundary layer. Unfortunately, free tropospheric measurements were not taken in EPIC2001 with the same frequency as boundary layer measurements, so there is less that we can say about the effects of the free tropospheric environment on convective forcing. However, a comparison between *Ron Brown* radiosonde soundings deployed respectively during periods of low and high

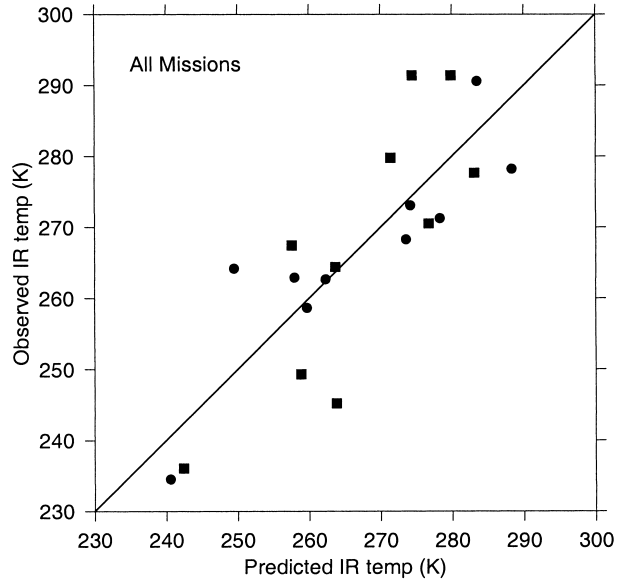


FIG. 19. Observed vs predicted infrared brightness temperature for all 20 EPIC2001 missions. The circles represent missions using C-130 dropsondes while the boxes represent those using P-3 dropsondes. The correlation coefficient is 0.82 and the correlation is significant at the 99% level.

infrared brightness temperature shows that soundings in active convective regions exhibit higher entropy aloft, and hence humidity (assuming unchanged temperature), than those in less active regions (see Fig. 20). On the other hand, very little difference is seen between the saturated entropy profiles, and hence temperature, between these two cases. It is unclear as to whether the higher humidity aloft contributes to the growth of the convection or is simply an artifact of its presence.

6. Conclusions

Observations made during the EPIC2001 project in the late summer and early fall of 2001 are used to infer those factors important to the initiation of deep convection in the ITCZ of the tropical eastern Pacific.

In-cloud measurements of deep convective updrafts reveal that these updrafts contain a mixture of air from the surface up to at least 900 mb. We found that developing deep convection occurs preferentially in locations in which a correspondingly deep layer is conditionally unstable. These locations tend to have values of satellite infrared brightness temperature which are rapidly decreasing with time, though the relation between brightness temperature tendency and deep conditional instability is somewhat noisy. Deep conditional instability is formalized in terms of small values of a deep convective inhibition index DCIN, which is equal to the average saturated moist entropy in the range 810–830 mb minus the average moist entropy in the range 900–1000 mb. Little sensitivity is found to the wind shear profile in convective initiation.

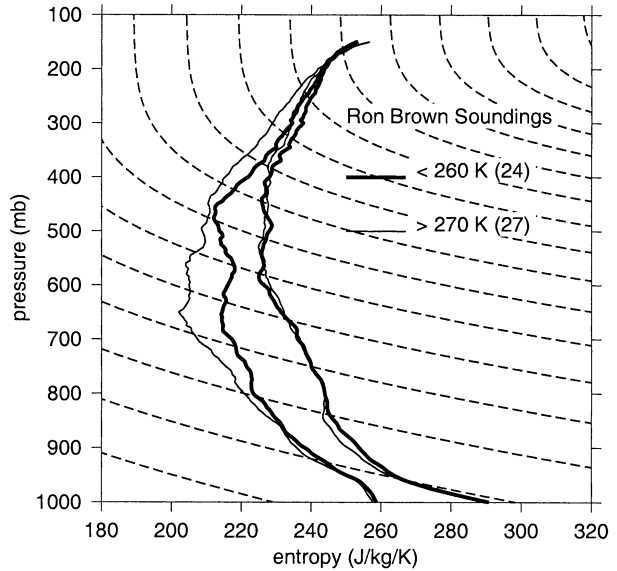


FIG. 20. Respective averages of *Ron Brown* soundings for mean infrared brightness temperatures in the ITCZ study region less than 260 K and greater than 270 K. The numbers in parentheses give the number of soundings in each average.

Since surface entropy fluxes increase the boundary layer entropy, they act to decrease the value of DCIN. One would therefore expect to see a correlation between stronger surface entropy fluxes and enhanced deep convection. Crude entropy budgets for the $4^\circ \times 4^\circ$ ITCZ study region confirm that the primary balance in this region is between surface fluxes and downdraft entropy fluxes. Daily averages of dropsonde-derived fluxes and nearby satellite infrared brightness temperatures are indeed correlated with a correlation coefficient over all 20 mission days of 0.66.

A number of cases are seen in which the surface fluxes are not in equilibrium with deep convection in the sense that the boundary layer entropy values are not large enough to result in small values of DCIN. This sometimes occurs because an inversion has developed in the 700–850-mb range, possibly as a result of large-scale subsidence, as observed previously in the eastern Pacific by Kloesel and Albrecht (1989).

DCIN itself does not correlate well with low infrared brightness temperatures, since convectively active regions tend to have both higher and lower than average values of DCIN (Raymond 1995; Kingsmill and Houze 1999b). However, DCINLOW, defined as the mean DCIN minus two standard deviations of the DCIN distribution, is correlated with infrared brightness temperature, with a correlation coefficient of 0.34 in our results. This makes sense because DCINLOW is an estimate of the most unstable DCIN values in the distribution. A joint regression of surface entropy flux and DCINLOW onto infrared brightness temperature over all EPIC2001 missions results in a correlation coefficient of 0.82, significant at the 99% level. Thus, fluctuations in surface entropy flux and DCINLOW

jointly account for $(0.82)^2 \approx 2/3$ of the variance in satellite infrared brightness temperature.

We emphasize that the above correlation is between domain-averaged quantities, as point values of infrared brightness temperature are not well correlated with corresponding surface entropy fluxes and DCIN values.

Presumably free tropospheric temperature, wind, and humidity profiles have an effect on deep convection in this region as well. Data from EPIC2001 are insufficient to test this hypothesis, though we do note a correlation in *Ron Brown* radiosonde soundings between low infrared brightness temperature and a moist middle to upper troposphere. However, we cannot determine whether this moisture is needed for the convection to develop or whether it is simply an artifact of its existence. More work is needed in this area.

The Mexican warm pool is a rather special area of the Tropics, similar in some ways to the western Pacific warm pool in that quiescent conditions with light winds are periodically interrupted by convective events exhibiting regions of strong surface winds. The applicability of the convective forcing model developed for the eastern Pacific needs to be tested in other regions with different wind regimes.

Acknowledgments. This project would have been impossible without the hard work of the UCAR Joint Office for Scientific Support, NCAR's Research Aviation Facility, NOAA's Aircraft Operations Center, and the faculty and staff of the Centro de Ciencias de la Atmósfera at the Universidad Nacional Autónoma de México (CCA-UNAM). The Colorado State University staff on the ship *Ron Brown* did an excellent job of deploying radiosondes. We also thank Darrel Baumgardner for computing the reflectivity-rainfall relationships for EPIC2001. Ed Zipser and two anonymous reviewers contributed significantly to this paper. Special thanks go to Jay Fein of the National Science Foundation (NSF) and Mike Patterson of NOAA's Office of Global Programs (OGP) for their dedicated support of EPIC2001. NSF and NOAA directly supported the deployment of the two aircraft and the two ships. NOAA's Pacific Marine Environmental Laboratory, which maintains the TAO mooring array, deployed three extra buoys and enhanced the instrumentation on all 95°W moorings for EPIC2001 with the support of NOAA/OGP. This work was sponsored by NSF Grants ATM-0082612, ATM-0082384, and ATM-0002387, and Consejo Nacional de Ciencia Y Tecnología (CONACyT) Grant 33319. The first author spent the academic year 2001–02 at CCA-UNAM in Mexico City with generous support from CONACyT.

APPENDIX

Aircraft Data Corrections

The NCAR Research Aviation Facility (RAF) compared the temperature and humidity of in situ sensors on the C-130 with three dropsondes deployed in close

proximity to descent and ascent soundings made by the aircraft. The heated Rosemount thermometer on the aircraft was found to be consistent with the dropsonde temperatures. However, the unheated Rosemount probes were found to have been damaged by ice during the project, resulting in changing calibration factors. For this reason the heated Rosemount was used as the reference temperature instrument throughout the project.

The aircraft humidities from the dewpoint instruments on the C-130 were found to be systematically low compared to the dropsondes. Laboratory measurements confirmed this bias. RAF therefore corrected the in situ humidities upward to match those of the dropsondes. The Lyman alpha hygrometer, adjusted for drifts by the corrected dewpoint measurements, was used as the reference measurement of humidity.

Two intercomparisons were made between the aircraft in missions 2 and 17 by flying wingtip to wingtip at three different pressure levels: 980, 810, and 640 mb. The corrected C-130 dewpoints agreed well with the P-3 dewpoints. However, the P-3 temperature tended to be slightly higher than the C-130 temperature, with a larger effect at lower pressures. Since the latter compared well with the dropsondes, the P-3 temperature was adjusted to match that of the C-130 according to the formula

$$T_{\text{cor}} = T - 0.3 - 0.2(980 - p)/360, \quad (\text{A1})$$

where the pressure p is in millibars and the temperature T is in degrees Celsius.

In-cloud temperature measurements were made on the C-130 using a radiometric thermometer constructed by the Ophir corporation. This instrument determines the temperature from the emissivity of the atmosphere in a carbon dioxide absorption band near 6.7 μm . Three problems had to be overcome to make the Ophir temperatures useful: 1) The radiometer output drifted slightly with time; 2) the radiometer view angle was depressed 20° below the horizontal plane of the aircraft, which means that photons from warmer air below the flight level were seen by the instrument even with the aircraft in straight and level flight; 3) the bandpass filter used to single out the carbon dioxide band was slightly too broad, so that a small fraction of the photons received in clear air came from as much as several kilometers away from the aircraft, thus contaminating the temperature measurement of the nearby air. In cloud, this contaminating effect is reduced or eliminated due to the large opacity of the cloud itself.

The last two points means that the temperature measured by the instrument is slightly higher outside of cloud than inside. This effect was confirmed by the observation that the difference between the in situ temperature and the radiometric temperature varied in a systematic way with aircraft roll angle. Since the Ophir is mounted so that it looks at right angles to the aircraft axis, rolling one way (to the right) causes the instrument to look down at an angle greater than 20° relative to

the horizon, thus seeing more deeply into the atmosphere below, while rolling the other way decreases this angle. Furthermore, this sensitivity to roll angle increases with altitude, since the atmosphere at higher levels becomes more transparent to infrared photons.

We made an empirical roll angle correction to the Ophir temperature based on the observation that the difference between the downward-pointing PRT-5 radiometer temperature and the in situ temperature in clear air exhibits approximately the same behavior with altitude as the roll sensitivity of the Ophir. To do this we assume that the Ophir gives us the correct temperature when the instrument is looking horizontally outward, a state of affairs which occurs when the aircraft is rolled 20° to the left. Thus, the quantity

$$\Delta T = A(R - R_0)(RSTB1 - ATX) \quad (A2)$$

is subtracted from the Ophir temperature, where R is the aircraft roll angle in degrees, $R_0 = -20^\circ$ is the roll angle that results in zero depression angle for the Ophir, $RSTB1$ is the PRT-5 temperature, and ATX is the in situ temperature. Note that this correction becomes small inside of cloud where $RSTB1 \approx ATX$. The coefficient $A = 0.00162$ was obtained by minimizing the overall roll sensitivity in clear air for many tests at various altitudes in which the aircraft was rolled from side to side. We estimate that the worst case error in this correction, which occurs at the highest altitudes, is about 0.5 K.

Once the above roll correction was done, we corrected for drift by forcing continuity between the Ophir and the heated Rosemount temperature a few seconds before entering and a few seconds after leaving cloud. This was done by adding the appropriate offset and linear trend to the Ophir temperature. We noticed that the heated Rosemount instrument seemed to recover from wetting and icing within a few seconds of emerging from cloud, whereas the nonheated Rosemounts took up to 30 s to recover under certain conditions. Thus, the heated Rosemount is a much better near-cloud reference for the Ophir than the nonheated immersion thermometers.

NCAR corrects C-130 inertial navigation system (INS) positions, groundspeeds, and winds for drift using global positioning system (GPS) data. As provided by NOAA, the P-3 INS positions are corrected for drift using GPS data, but the aircraft ground speeds and computed winds are not. We corrected P-3 ground speeds for INS drift by adding the high-frequency part of the INS ground speed to the low-frequency part of the GPS ground speed. The cutoff frequency for both filters was $(250 \text{ s})^{-1}$. Since the horizontal wind velocity \mathbf{v} relative to the earth is computed using

$$\mathbf{v} = \mathbf{a} + \mathbf{g}, \quad (A3)$$

where \mathbf{a} is the horizontal wind relative to the aircraft and \mathbf{g} is the horizontal velocity of the aircraft relative

to the ground, a GPS-corrected horizontal wind may be obtained from

$$\mathbf{v}_{\text{cor}} = \mathbf{v} - \mathbf{g}_{\text{ins}} + \mathbf{g}_{\text{cor}}, \quad (A4)$$

where \mathbf{g}_{cor} is the GPS-corrected ground velocity, and \mathbf{g}_{ins} is the uncorrected INS ground velocity.

Even with the above GPS corrections, the intercomparison flights showed a significant discrepancy between C-130 and P-3 winds. This discrepancy was traced to a difference in measured true airspeeds between the aircraft while flying in close formation. The C-130 executed calibration maneuvers during the project, including a reverse track maneuver, which is designed to detect errors in the true airspeed measurement. We therefore assume that the C-130 true airspeed is more nearly correct and adjust the P-3 true airspeed to match it. The best match was obtained by multiplying the P-3 true airspeed by the factor 1.014 . This factor was applied to the air velocity calculation by first computing the uncorrected wind relative to the aircraft from the ground speed and the uncorrected airspeed:

$$\mathbf{a} = \mathbf{v} - \mathbf{g}. \quad (A5)$$

This velocity was then corrected using

$$\mathbf{a}_{\text{cor}} = 1.014\mathbf{a}. \quad (A6)$$

Finally the corrected wind was computed using

$$\mathbf{v}_{\text{cor}} = \mathbf{a}_{\text{cor}} + \mathbf{g}. \quad (A7)$$

When both corrections (A4) and (A7) are applied, the C-130 and P-3 winds agree with each other to better than 0.5 m s^{-1} for both intercomparison flights.

The P-3 GPS receiver gave unreliable measurements for a segment of the mission 2 flight for unknown reasons. During this interval the GPS-corrected ground velocity and winds were replaced by the uncorrected winds. However, as this flight segment was early in the flight, the INS drifts were small, and the errors thereby introduced are small.

REFERENCES

- Bister, M., and K. A. Emanuel, 1997: The genesis of Hurricane Guillermo: TEXMEX analyses and a modeling study. *Mon. Wea. Rev.*, **125**, 2662–2682.
- Emanuel, K. A., 1986: An air–sea interaction theory for tropical cyclones. Part I: Steady-state maintenance. *J. Atmos. Sci.*, **43**, 585–604.
- , 1994: *Atmospheric Convection*. Oxford University Press, 580 pp.
- , 1995: The behavior of a simple hurricane model using a convective scheme based on subcloud-layer entropy equilibrium. *J. Atmos. Sci.*, **52**, 3960–3968.
- Firestone, J., and B. A. Albrecht, 1986: The structure of the atmospheric boundary layer in the central equatorial Pacific during FGGE. *Mon. Wea. Rev.*, **114**, 2219–2231.
- Jorgensen, D. P., and P. T. Willis, 1982: A Z–R relationship for hurricanes. *J. Appl. Meteor.*, **21**, 356–366.
- , T. R. Shepherd, and A. S. Goldstein, 2000: A dual-pulse repetition frequency scheme for mitigating velocity ambiguities of

- the NOAA P-3 airborne Doppler radar. *J. Atmos. Oceanic Tech.*, **17**, 585–594.
- Kingsmill, D. E., and R. A. Houze Jr., 1999a: Kinematic characteristics of air flowing into and out of precipitating convection over the west Pacific warm pool: An airborne Doppler radar survey. *Quart. J. Roy. Meteor. Soc.*, **125**, 1165–1207.
- , and —, 1999b: Thermodynamic characteristics of air flowing into and out of precipitating convection over the west Pacific warm pool. *Quart. J. Roy. Meteor. Soc.*, **125**, 1209–1229.
- Kloesel, K. A., and B. A. Albrecht, 1989: Low-level inversions over the tropical Pacific—Thermodynamic structure of the boundary layer and the above-inversion moisture structure. *Mon. Wea. Rev.*, **117**, 87–101.
- LeMone, M. A., E. J. Zipser, and S. B. Trier, 1998: The role of environmental shear and thermodynamic conditions in determining the structure and evolution of mesoscale convective systems during TOGA COARE. *J. Atmos. Sci.*, **55**, 3493–3518.
- Lindzen, R. S., and S. Nigam, 1987: On the role of sea surface temperature gradients in forcing low-level winds and convergence in the Tropics. *J. Atmos. Sci.*, **44**, 2418–2436.
- Lucas, C., and E. J. Zipser, 2000: Environmental variability during TOGA COARE. *J. Atmos. Sci.*, **57**, 2333–2350.
- , —, and B. S. Ferrier, 2000: Sensitivity of tropical west Pacific oceanic squall lines to tropospheric wind and moisture profiles. *J. Atmos. Sci.*, **57**, 2351–2373.
- Malkus, J., and H. Riehl, 1960: On the dynamics and energy transformations in steady-state hurricanes. *Tellus*, **12**, 1–20.
- Mapes, B. E., 1993: Gregarious tropical convection. *J. Atmos. Sci.*, **50**, 2026–2037.
- McPhaden, M. J., 1995: The tropical atmosphere ocean array is completed. *Bull. Amer. Meteor. Soc.*, **76**, 739–741.
- Paluch, I. R., G. McFarquhar, D. H. Lenschow, and Y. Zhu, 1999: Marine boundary layers associated with ocean upwelling over the eastern equatorial Pacific Ocean. *J. Geophys. Res.*, **104**, 30 913–30 936.
- Parsons, D. B., K. Yoneyama, and J.-L. Redelsperger, 2000: The evolution of the tropical western Pacific atmosphere–ocean system following the arrival of a dry intrusion. *Quart. J. Roy. Meteor. Soc.*, **126**, 517–548.
- Raymond, D. J., 1995: Regulation of moist convection over the west Pacific warm pool. *J. Atmos. Sci.*, **52**, 3945–3959.
- , and A. M. Blyth, 1992: Extension of the stochastic mixing model to cumulonimbus clouds. *J. Atmos. Sci.*, **49**, 1968–1983.
- , C. López-Carrillo, and L. López Cavazos, 1998: Case-studies of developing east Pacific easterly waves. *Quart. J. Roy. Meteor. Soc.*, **124**, 2005–2034.
- Reynolds, R. W., 1988: A real-time global sea surface temperature analysis. *J. Climate*, **1**, 75–86.
- , and D. C. Marsico, 1993: An improved real-time global sea surface temperature analysis. *J. Climate*, **6**, 114–119.
- Riehl, H., T. C. Yeh, J. S. Malkus, and N. E. La Seur, 1951: The north-east trade of the Pacific Ocean. *Quart. J. Roy. Meteor. Soc.*, **77**, 598–626.
- Rotunno, R., and K. A. Emanuel, 1987: An air–sea interaction theory for tropical cyclones. Part II: Evolutionary study using a non-hydrostatic axisymmetric numerical model. *J. Atmos. Sci.*, **44**, 542–561.
- Saxen, T. R., and S. A. Rutledge, 1998: Surface fluxes and boundary layer recovery in TOGA COARE: Sensitivity to convective organization. *J. Atmos. Sci.*, **55**, 2763–2781.
- Yin, B., and B. A. Albrecht, 2000: Spatial variability of atmospheric boundary layer structure over the eastern equatorial Pacific. *J. Climate*, **13**, 1574–1592.
- Yoneyama, K., and D. B. Parsons, 1999: A proposed mechanism for the intrusion of dry air into the tropical western Pacific region. *J. Atmos. Sci.*, **56**, 1524–1546.
- Zipser, E. J., 1969: The role of organized unsaturated convective downdrafts in the structure and rapid decay of an equatorial disturbance. *J. Appl. Meteor.*, **8**, 799–814.
- , 1977: Mesoscale and convective-scale downdrafts as distinct components of squall-line structure. *Mon. Wea. Rev.*, **105**, 1568–1589.